ChemPubSoc Europe

DOI: 10.1002/cphc.201701214

CHEMPHYSCHEM Articles

Laser-Assisted Synthesis of Colloidal FeW_xO_y and Fe/Fe_xO_y Nanoparticles in Water and Ethanol

Niusha Lasemi,[a] Oscar Bomatí Miguel,*[a, b] Ruth Lahoz,[c] Vassili. V. Lennikov,[d] Ulrich Pacher,[a] Christian Rentenberger,[e] and Wolfgang Kautek*[a]

Homogeneous polycrystalline Fe_xO_y nanoparticles were generated by ablation of iron targets in water by nanosecond laser pulses at 532 nm. In ethanol, crystalline core-shell Fe/Fe_xO_y structures with size medians around 20 nm were produced. The ablation of FeW_xO_y targets in water resulted in crystalline hollow shells and homogeneous FeW_xO_y nanoparticles. In contrast, amorphous core-shell FeW_xO_y nanoparticles with a median size of 17 nm were produced in ethanol. The size distribution of both the Fe_xO_y and the FeW_xO_y particles showed a slight dependence on fluence and pulse number. This may be related to primary and secondary ablation and modification mechanisms.

1. Introduction

The laser-assisted generation of nanoparticles (NPs) in liquids involves numerous processes taking place in the solid, such as absorption, electron-phonon coupling, incubation,[1] in the interfacial region, e.g. mixed phase and cavitation bubble formation,[2] and in the liquid bulk, secondary laser particle interactions.[3] Size, shape and the core-shell morphology can be controlled by the laser parameters and the nature of the fluid. Laser ablation synthesis in solutions (LASiS) can be regarded as a green method to produce noble metal nanoparticles without any chemical stabilizers.[1c,4] Also industrial catalysis requires fully accessible surface atoms free from surface active agents.[5] In medical applications, e.g. stabilizers such as thiols and disulfides may show lethal potential in destroying red blood cells.[6] LASiS promises the avoidance of possibly toxic surfactants and additives for colloidal solutions that cannot be reached by conventional manufacturing routs. In this context, the laser ablation of Ni, Fe, and W oxide NPs from metallic targets in water and alcohol were studied systematically.[1d]

Magnetic nanoparticles (MNPs) reveal remarkable properties in biomedical applications such as nanoantibiotic therapy, cancer diagnosis, non-invasive cell tracking, labelling, stimulating stem cells, and monitoring in-vitro/in-vivo behaviour.[7] In this context, particularly the laser generation of iron oxide NPs attracted attention[7f,8] due to their outstanding properties such as biocompatibility and biodegradability.[9] Superparamagnetic iron oxide nanoparticles were used as an effective contrast agent (CA) in magnetic resonance imaging (MRI) for in vivo cell tracking and cell labelling without any cellular destruction.[10] Superparamagnetic behaviours can experimentally be observed in Fe NPs with sizes of between 10–24 nm.[11] Interestingly iron oxide NPs behave as a negative CA and show hypointense contrast.[12] Moreover, iron-based CAs per mole exhibit generally stronger contrast in MRI than the common Gd(III) chelates.[13] Smaller sizes (30–50 nm), i.e. USPIOs, allow prolonged blood circulation time and better chance in crossing tumor vessel wall.[14]

Moderate attention, however, was given to nanoalloys in medical science due to many unanswered questions with respect to biocompatibility, cytotoxicity, chemical activity and stability over time.[7a,15] Most of the available *T*1 (spin-lattice relaxation time) CAs are paramagnetic compounds and those categorized as *T*2 (spin-spin relaxation time) CAs are superparamagnetic iron oxides NPs.[16] Bimetallic nanoparticles (BNPs) attracted attention in medical and technological applications.[15e,17] In all cases, Fe oxide was one of the components such as Fe–Co,[18] Fe–Bi,[19] Fe–Ni,[20] Fe–Pt,[21] and the ferrites $MnFe_2O_4$[22] and $CoFe_2O_4$.[23] Recently, LASiS of some bimetallic NPs were reported.[24]

Dual mode W–Fe NPs were synthesized conventionally.[25] Since tungsten is a paramagnetic element, its combination with iron oxide may form potential dual mode CAs for ultrahigh field MRI and X-ray computed tomography.

In the present work, LASiS of Fe/Fe_xO_y NPs from a pure metal target and a potential dual mode CA, i.e. FeW_xO_y, from the respective ceramic alloy target is reported. The influence of the laser fluence, the pulse number, and the nature of the liquid, water and ethanol, on the size distribution and the NP structure is discussed.

[a] Dr. N. Lasemi, Prof. Dr. O. Bomatí Miguel, U. Pacher, Prof. Dr. W. Kautek
University of Vienna, Department of Physical Chemistry
Währinger Strasse 42, A-1090 Vienna (Austria)
E-mail: wolfgang.kautek@univie.ac.at
oscar.bomati@uca.es
[b] Prof. Dr. O. Bomatí Miguel
Universidad de Cádiz, Departamento de Física de la Materia Condesada, Ancha 16, E-11001 Cádiz (Spain)
[c] Dr. R. Lahoz
University of Zaragoza – CSIC, Centro de Química y Materiales de Aragón, María de Luna 3, E-50018, Zaragoza (Spain)
[d] Dr. V. V. Lennikov
University of Zaragoza – CSIC, Instituto de Ciencia de Materiales de Aragón, María de Luna 3, E-50018, Zaragoza (Spain)
[e] Prof. C. Rentenberger
University of Vienna, Faculty of Physics
Boltzmanngasse 5, A-1090 Vienna (Austria)

2. Results and Discussion

LASiS of Fe targets in water yielded NPs with sizes more than about 20 nm. Diffraction patterns (SAED) indicated polycrystalline NPs consisting of some metallic iron and various oxidic phases such as Fe_2O_3 and Fe_3O_4 (Figure 1, Table 1). The bright field image shows crystal defects common for cubic structures. There is no indication for shell phases.

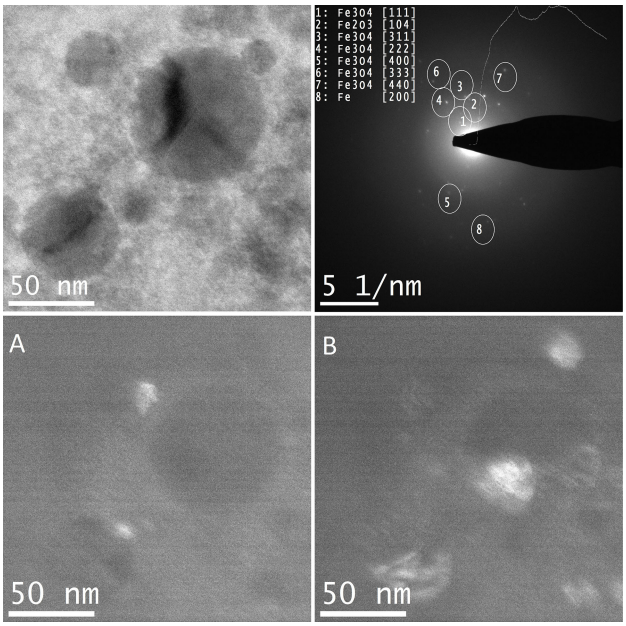

Figure 1. Fe_xO_y NPs laser-synthesized in water. $N=200$, $F=1900$ Jcm^{-2}. Bright field image (upper left), selected area diffraction pattern (SAED; upper right). Respective dark-field images at various tilting angles (A, B).

LASiS in ethanol led to core-shell structures (Figure 2). The number weighted size distribution of the Fe NPs generated in ethanol at a pulse number $N=200$ is slightly bimodal with medians around 17 and 24 nm (Figure 2, Table 2).

The bright field image and the selected area diffraction pattern (SAED) with a contrast aperture at positions A1 and A2, and the corresponding dark field images (A1, A2) of Fe NPs laser-synthesized in ethanol indicate core-shell structures (Figure 3).

The crystallographic data and phase identifiers are summarized in (Table 3). Contrast Aperture A1 corresponds to an Fe

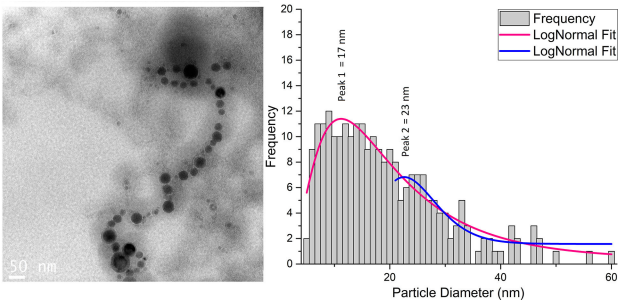

Figure 2. Fe/Fe_xO_y NPs laser-synthesized in ethanol. TEM image and size distribution (number weighted). $N=200$. $F=1900$ Jcm^{-2}.

Table 2. Fe/Fe_xO_y NPs laser-synthesized in ethanol. Fitting results of number weighted size distribution. $N=200$. $F=1900$ Jcm^{-2}.

Curve Fitting (Log-normal)	Median [nm]	Mean [nm]	Standard Deviation
1	17.4 ± 0.5	21.7 ± 0.5	16.17
2	23.7 ± 0.5	24.3 ± 0.5	5.57

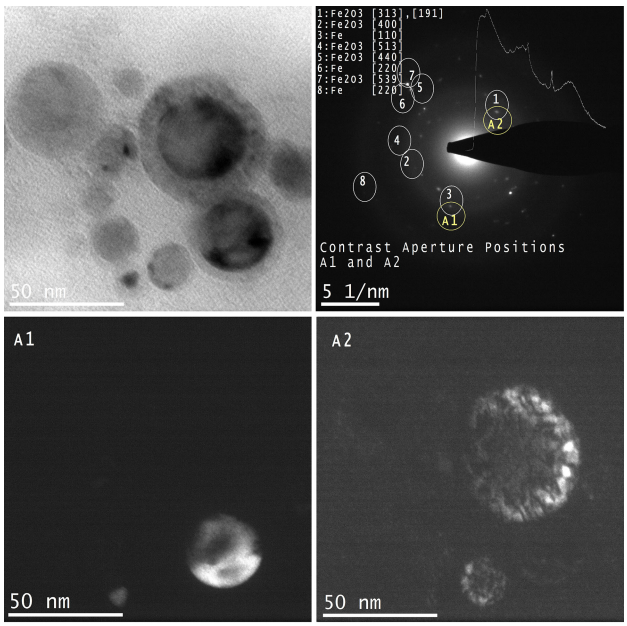

Figure 3. Fe/Fe_xO_y NPs laser-synthesized in ethanol. Bright-field image (upper left) and selected area diffraction pattern (SAED) with a contrast aperture at marked positions A1 and A2 (upper right). Respective dark-field images A1 and A2 (bottom). $N=200$, $F=1900$ Jcm^{-2}.

Table 1. Fe_xO_y NPs laser-synthesized in water. Selected area diffraction pattern (SAED) results, crystallographic data, and phase identifiers. $N=200$, $F=1900$ Jcm^{-2}.

Material	Mineral Name	Crystal System	Miller Indices	Pearson Symbol	Space Group	Space Group Number
Fe_3O_4	Magnetite	Cubic	[111]	cF56	Fd-3m	227
α-Fe_2O_3	Hematite	Hexagonal	[104]	hR30	R-3c	167
Fe_3O_4	Magnetite	Cubic	[311]	cF56	Fd-3m	227
Fe_3O_4	Magnetite	Cubic	[222]	cF56	Fd-3m	227
Fe_3O_4	Magnetite	Cubic	[400]	cF56	Fd-3m	227
Fe_3O_4	Magnetite	Cubic	[333]	cF56	Fd-3m	227
Fe_3O_4	Magnetite	Cubic	[440]	cF56	Fd-3m	227
Fe	–	Cubic	[200]	cI2	Im-3m	229

Table 3. Fe/Fe_xO_y NPs laser-synthesized in ethanol. Selected area diffraction pattern (SAED) results, crystallographic data, and phase identifiers. $N = 200$, $F = 1900$ Jcm^{-2}.

Material	Crystal System	Miller Indices	Pearson Symbol	Space Group	Space Group Number
Fe_2O_3	Tetragonal	[313], [119]	tP160	$P4_12_12$	92
Fe_2O_3	Tetragonal	[400]	tP160	$P4_12_12$	92
Fe	Cubic	[110]	cI2	Im-3m	229
Fe_2O_3	Tetragonal	[513]	tP160	$P4_12_12$	92
Fe_2O_3	Tetragonal	[440]	tP160	$P4_12_12$	92
Fe	Cubic	[220]	cF4	Fm-3m	225
Fe_2O_3	Tetragonal	[539]	tP160	$P4_12_12$	92
Fe	Cubic	[220]	cI2	Im-3m	229

[110] bcc pattern, the position of the A2 aperture is related to Fe_2O_3 [513] of the tetragonal system (Figure 3). The dark field images at various aperture positions indicate the core-shell structure and the composition. Contrast aperture position A1 shows that the core is crystalline Fe. Position A2 indicates a shell consisting of crystalline Fe_2O_3. Laser synthesized Fe targets in ethanol lead to core-shell Fe/Fe_2O_3 NPs with tetragonal Fe_2O_3 phase. The tetragonal phase may originate from a distortion of the Fe bcc structure due to internal strain.[26]

The increase of the fluence F (Figure 4) shows an influence on the size distribution (Table 4). The median size and the size

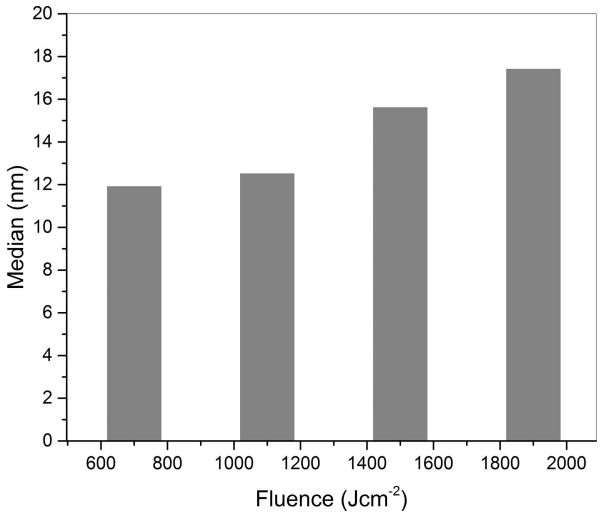

Figure 4. Median size diameters of Fe/Fe_xO_y NPs versus laser fluences in ethanol at $N = 200$.

distribution width increased with higher F and N. This is in accordance with the former LASiS results of Ni oxide,[1c] Fe oxide,[27] Cu oxide,[28] and Zn oxide[29] NPs.

Secondary processes such as post-irradiation of NPs generated by previous pulses complicate the mechanism of the NP generation, and should be considered together with the primary steps of the target ablation.[2b,30]

Fe NPs showed a slight bimodal size distribution in analogy with laser-synthesized Ni[1c] and Au[2a] NPs. The bimodal characteristics can be correlated to the generation processes taking place in and next to hemi-spherical cavitation bubble.[2a,b] When cavitation bubbles reach their maximum size, two distinguishable NP sizes may be observed.[2a] Primary Au NPs[2a] of 8–10 nm, e.g., were dispersed all over the bubble volume. A higher density of larger NPs was observed at the bottom of the bubble which decayed towards the top of the bubble. The smaller NPs can penetrate the bubble interface before its collapse.[2a,b,30c] Secondary NPs of around 45–50 nm due to collisions of primary particles trapped within the bubble reached a maximum density at the upper part of the bubble.[2a,b] Recoil pressure in high density liquids may play a role to increase the ablation rate and decrease the threshold fluence based on a high vapour pressure and temperature at the molten surface under higher confinement conditions.[31] Higher large NP-concentration may also lead to faster coalescence and Ostwald ripening.[32] The most recent concept of these complicated conditions suggests a primary ablation mechanism in a low density metal-water mixing region at moderate fluences yielding small NPs, whereas a superheated molten metal layer becomes disintegrated to larger NPs at higher fluences.[3b]

The mixed FeW_xO_y NPs were laser-generated from laser-sintered oxide targets. Selected area diffraction patterns of the FeW_xO_y NPs in water yielded crystallographic data and phase identifiers for a sample area with 60 μm diameter (Table 5).

In singular cases of large FeW_xO_y NPs greater than 100 nm, no signal could be detected related to cores when generated in water (Figure 5). Contrast aperture positons of A1, A2, A3 and the respective dark field images are depicted there. Even amorphous structures should show speckle contrasts especially

Table 4. Size distribution of laser-synthesized Fe/Fe_xO_y NPs in ethanol. The first fitting curve is log-normal.

F [Jcm^{-2}]	N	Median [nm]	Mean [nm]	Standard Deviation	F [Jcm^{-2}]
1900	200	17.4 ± 0.5	21.7 ± 0.5	16.17	1900
1500	200	15.6 ± 0.5	17.7 ± 0.5	9.64	1500
1100	200	12.5 ± 0.5	14.2 ± 0.5	7.75	1100
700	200	11.9 ± 0.5	14.3 ± 0.5	9.46	700

Table 5. FeW_xO_y NPs laser-synthesized in water. Selected area diffraction pattern (SAED) results, crystallographic data, and phase identifiers. $N = 200$, $F = 1900\ Jcm^{-2}$.

Material	Lattice Distance [nm]	Mineral Name	Crystal System	Miller Indices	Pearson Symbol	Space Group Number
WFe_2O_6	0.2882	–	Orthorhombic	[131]	oP36	60
FeO [OH]	0.2481	–	Orthorhombic	[110]	oP6	31
$WFeO_4$	0.2482	Ferberite	Orthorhombic	[002]	mP12	13
FeO [OH]	0.2483	–	–	[330]	tI24	87
WFe_2O_6	0.2483	–	Orthorhombic	[002]	oP36	60
Fe_2O_3	0.2485	–	Orthorhombic	[200]	oP20	62
FeO	0.2489	Wüstite	Cubic	[111]	cF8	225
FeO [OH]	0.2022	–	Orthorhombic	[021]	oP6	31
Fe	0.2027	–	Cubic	[110]	cI2	229
Fe_2O_3	0.2026	–	Hexagonal	[106],[016]	hP30	143
Fe_2O_3	0.2029	–	Hexagonal	[114],[11$\bar{4}$]	hP30	143
W_3O_8	0.1613	–	–	[132]	oS22	21
W_3O_8	0.1613	–	Orthorhombic	[322]	oP44	55
Fe_3O_4	0.1616	Magnetite	Cubic	[333],[511]	cF56	227
WO_3	0.1491	–	Monoclinic	[311],[34$\bar{3}$], [13$\bar{5}$]	mP32	14
α-Fe_2O_3	0.1492	Hematite	Hexagonal	[214],[12$\bar{4}$]	hR30	167
WFe_2O_6	0.1499	–	Orthorhombic	[133]	oP36	60
WO_2	0.1404	–	Orthorhombic	[313]	oP36	62
WO_2	0.1409	–	Monoclinic	[131]	mP12	14
FeO	0.1300	Wüstite	Cubic	[311]	cF8	225
W	0.1303	–	Cubic	[211]	cI2	229
FeO	0.1244	Wüstite	Cubic	[222]	cF8	225
α-Fe_2O_3	0.1061	Hematite	Hexagonal	[121$\bar{0}$], [2110]	hR30	167
Fe	0.1063	–	Hexagonal	[200]	hP2	194
WO_3	0.1065	–	Cubic	[320]	cP4	221
Fe	0.0940	–	Cubic	[400]	cF4	225
WO_3	0.0905	–	Cubic	[330],[411]	cP4	221
Fe	0.0906	–	Cubic	[310]	cI2	229
WO_3	0.0907	–	Tetragonal	[442]	tP161	130

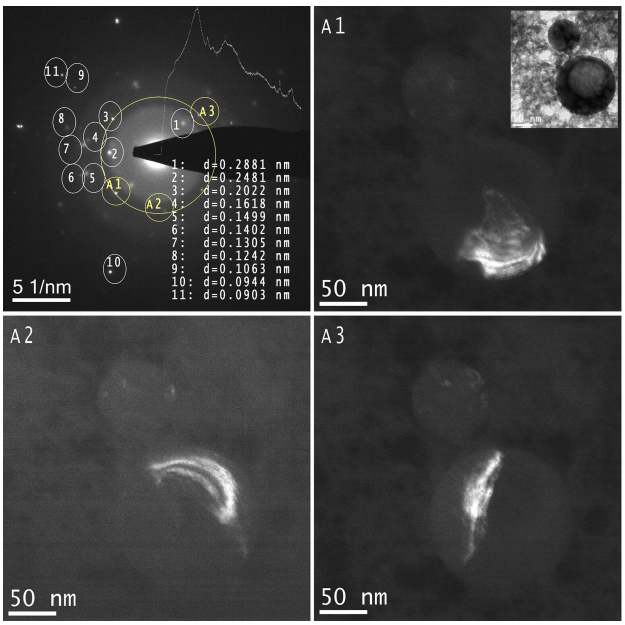

Figure 5. FeW_xO_y NPs laser-synthesized in water. Selected area diffraction pattern (SAED) with a contrast aperture at marked positions A1, A2, A3 (upper left). Respective dark-field images A1, A2, A3. $N = 200$, $F = 1900\ Jcm^{-2}$.

in dark-field images. Therefore, hollow cores may be assumed. The mechanism of formation of hollow core-shell NPs can be described as so called Kirkendall effect in which the atomic inter-diffusion at the interface of two metals can occur through a vacancy exchange mechanism.[33] Unbalanced diffusion rates between two stacked metals may lead to vacancies and finally voids in the interface region. These phenomena need further investigations.

The crystallographic data, and phase identifiers with all possible crystal systems for the calculated lattice distances are summarized in Table 5. The dark field images related to the contrast aperture positions A1 to A3 on the large ring in Figure 5 show crystalline shell structures consisting of Fe_2O_3 or/and FeO(OH) (Table 5).

Laser generation from the FeW_xO_y target in ethanol led to core-shell NPs (Figure 6). The selected area diffraction pattern (SAED) only indicated amorphous phases.

A slightly bimodal size distribution with median sizes of ~13 nm and ~20 nm was observed (Table 6). The median size increased from 13 nm to 20 nm with increasing *F*, which represents an analogous trend to the fluence dependence of the size distribution of the iron oxide NPs (Table 4). This behaviour can be rationalized as in the case of Fe NPs generated in the same solvent (Figure 2, Table 2).

3. Conclusions

Fe_xO_y NPs laser synthesized from Fe targets in water show homogeneous and polycrystalline oxidic phases such as Fe_2O_3 and Fe_3O_4. The generation in ethanol led to crystalline core-shell Fe/Fe_2O_3 structures with size medians around 20 nm. The median size and the size distribution width increased with higher fluence and pulse number due to either primary ablation

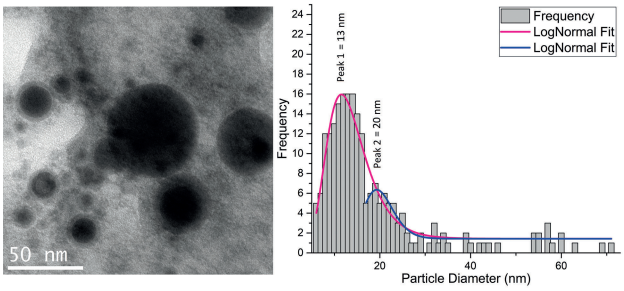

Figure 6. FeW_xO_y NPs laser-synthesized in ethanol. TEM image and size distribution (number weighted). $N = 200$. $F = 1900\ Jcm^{-2}$.

Table 6. FeW_xO_y NPs laser-synthesized in ethanol. Fitting results of the number-weighted size distribution. $N = 200$. $F = 1900 Jcm^{-2}$.

Curve Fitting (Log-normal)	Median [nm]	Mean [nm]	Standard Deviation
1	13.0 ± 0.5	13.8 ± 0.5	5.05
2	19.8 ± 0.5	20.1 ± 0.5	3.31

processes and/or secondary types such as coalescence and Ostwald ripening. A primary ablation mechanism may also depend on these parameters. A low density metal-water mixing region may be generated at moderate fluences yielding small NPs, whereas a superheated molten metal layer becomes disintegrated to larger NPs at higher fluences.

The FeW_xO_y NPs synthesized in water show mixtures of Fe_xO_y, FeO(OH) and also phases of FeW_xO_y. In some cases, hollow crystalline shells consisting of Fe_2O_3 or/and FeO(OH) occurred. Laser generation in ethanol led to amorphous core-shell FeW_xO_y NPs. The size distribution showed a median size of 13 nm at moderate fluences.

Experimental Section

The target materials were round iron (diameter 15 mm, thickness 0.5 mm) and iron-tungsten oxide ceramic disks (diameter 10 mm, thickness 1.5 mm). They were prepared by superficial laser melt mixing of raw ceramic tiles with a diode-pumped Nd:YAG laser (Powerline E20, Rofin) delivering pulses of ca. 50 ns pulse width. The laser heads were fitted with a galvanometer beam steering system and coupled to a flat-field lens of 160 mm focal distance providing a spot size of ca. 30 μm. The pulse repetition rates ranged from 20 to 200 kHz, at output power values from 0.1 to 20 W. These conditions resulted in irradiance values between 0.5 and 100 MW/cm^2. Scanning rates were varied between 500 and 3000 mm/s.

The liquids for the NP generation were distilled water and ethanol (Sigma-Aldrich; p.a.). A Q-switched Nd:YAG Laser system was employed emitting at a wavelength of 532 nm (Spectra Physics GCR-130, $\leq$1.2 W, pulse duration 5 ns, repletion rate 20 Hz, beam diameter ca. 5 mm). The metal targets were positioned in a glass cell with an optical window allowing the horizontal access of the laser beam. This was focused by a plano-convex lens with a focal length of 92 mm yielding a depth of focus (DOF) of 1.5 mm. Thus, the DOF was much greater than the maximum peak-to-valley distance of the target roughness features (ca. 120 μm). That means that the sample roughness had no influence on the spot size and therefore the evaluated fluence values. The cell was positioned on a motorized XY-scanning stage. The energy attenuation was performed by a polarizer with a half-wave plate. The power meter (OPHIR Photonics) was positioned after the polarizer (THORLABS). The focus position in air and in various liquid media were experimentally evaluated by microscopically measuring the ablation area on a silicon target (OLYMPUS, STM-MJS microscope; Zeiss AxioVision software) as a function of the distance of the focusing plano-convex lens. The images of the modified sample target regions were recorded by a CCD camera connected to the optical microscope and were evaluated (Zeiss AxioVision software). From this, the average diameter D and D^2, respectively, were calculated in order to evaluate the (D^2-ln$F$)-relationship.[34] From this, the Gaussian beam radius could be derived and compared with measurements according to the so-called cutting edge technique[35].

The size distribution and electron diffraction patterns of the laser-synthesized NPs were studied by transmission electron microscopy (Philips CM200 TEM; LaB6 cathode, acceleration voltage of 200 kV). The TEM images and the selected area electron diffraction (SAD) patterns were recorded by a Gatan Orius CCD camera. The size distribution was evaluated from at least six TEM frames (700 × 700 nm) by the microscopy software (Gatan, Inc.). The analysing parameters of electron diffraction patterns were calculated by intensity profile analysis selected area diffraction (PASAD; University of Vienna, C. Gammer)[36] and microscopy software (Gatan, Inc.). The crystallographic data and phase identification of the NPs was performed by means of the AtomWork database.[37] Energy-dispersive X-ray spectroscopy (EDX) in connection with TEM served for chemical composition investigations. The NP samples for the TEM investigation were prepared by placing a droplet of the colloidal dispersion (after 5 min ultrasonic irradiation) on a carbon-film-coated copper grid followed by the solvent evaporation in air at room temperature.

Acknowledgements

Partial financial support by the H2020 Action MSCA-IF 656908-NIMBLIS-ESR is acknowledged. Further partial funding came from the National Science Foundation through Grant CMMI-1301298, and the MAT2015-67354-R project of the Spanish Ministry of Economy and Competitiveness (MINECO). The authors are grateful to Prof. G.F. de la Fuente (Instituto de Ciencia de Materiales de Aragón, CSIC-Universidad de Zaragoza, Spain) for support in the preparation of the iron-tungsten ceramic targets.

Conflict of Interest

The authors declare no conflict of interest.

Keywords: colloids · core-shell structure · iron · laser ablation synthesis in solution (LASiS) · nanoparticles

[1] a) D. Bäuerle, *Laser processing and chemistry*, 4 ed., Springer-Verlag Berlin Heidelberg, **2011**; b) C.-Y. Shih, M. V. Shugaev, C. Wu, L. V. Zhigilei, *J. Phys. Chem. C* **2017**, *121*, 16549–16567; c) N. Lasemi, U. Pacher, C. Rentenberger, O. Bomatí-Miguel, W. Kautek, *ChemPhysChem* **2017**, *18*, 1118–1124; d) N. Lasemi, U. Pacher, L. V. Zhigilei, O. Bomatí-Miguel, R. Lahoz, W. Kautek, *Appl. Surf. Sci.* **2018**, *433*, 772–779.

[2] a) S. Ibrahimkutty, P. Wagener, A. Menzel, A. Plech, S. Barcikowski, *Appl. Phys. Lett.* **2012**, *101*, 103104; b) P. Wagener, S. Ibrahimkutty, A. Menzel, A. Plech, S. Barcikowski, *Phys. Chem. Chem. Phys.* **2013**, *15*, 3068–3074; c) A. De Giacomo, M. Dell'Aglio, A. Santagata, R. Gaudiuso, O. De Pascale, P. Wagener, G. C. Messina, G. Compagnini, S. Barcikowski, *Phys. Chem. Chem. Phys.* **2013**, *15*, 3083–3092.

[3] a) J. Lam, D. Amans, F. Chaput, M. Diouf, G. Ledoux, N. Mary, K. Masenelli-Varlot, V. Motto-Ros, C. Dujardin, *Phys. Chem. Chem. Phys.* **2014**, *16*, 963–973; b) C.-Y. Shih, C. Wu, M. V. Shugaev, L. V. Zhigilei, *J. Colloid Interface Sci.* **2016**.

[4] a) P. P. Patil, D. M. Phase, S. A. Kulkarni, S. V. Ghaisas, S. K. Kulkarni, S. M. Kanetkar, S. B. Ogale, V. G. Bhide, *Phys. Rev. Lett.* **1987**, *58*, 238–241; b) F. Mafune, J.-y. Kohno, Y. Takeda, T. Kondow, H. Sawabe, *J. Phys. Chem. B* **2000**, *104*, 9111–9117; c) A. V. Kabashin, M. Meunier, *J. Appl. Phys.* **2003**, *94*, 7941–7943; d) M. Brikas, S. Barcikowski, B. Chichkov, G. Račiukaitis, *JLMN* **2007**, *2*, 230–233; e) V. Amendola, M. Meneghetti, *Phys. Chem. Chem. Phys.* **2009**, *11*, 3805–3821; f) S. C. Singh, H. B. Zeng, C. Guo, W. Cai, *Nanomaterials: Processing and Characterization with Lasers*, Wiley-VCH publication, **2012**; g) G. Yang, *Laser Ablation in Liquids, Principles and Applications in the Preparation of Nanomaterials*, Pan Stanford Publishing, **2012**; h) S. Barcikowski, G. Compagnini, *Phys. Chem. Chem. Phys.* **2013**, *15*, 3022–3026.

[5] a) G. Merga, L. C. Cass, D. M. Chipman, D. Meisel, *J. Am. Chem. Soc.* **2008**, *130*, 7067–7076; b) A. Corma, H. Garcia, *Chem. Soc. Rev.* **2008**, *37*, 2096–2126.

[6] a) M.-C. Daniel, D. Astruc, *Chem. Rev.* **2004**, *104*, 293–346; b) P. G. Etchegoin, E. C. Le Ru, *Phys. Chem. Chem. Phys.* **2008**, *10*, 6079–6089.

[7] a) S. Laurent, D. Forge, M. Port, A. Roch, C. Robic, L. Vander Elst, R. N. Muller, *Chem. Rev.* **2008**, *108*, 2064–2110; b) H. Markides, M. Rotherham, A. J. El Haj, *J. Nanomater.* **2012**, *2012*, 11; c) W. Zhang, X. Shi, J. Huang, Y. Zhang, Z. Wu, Y. Xian, *ChemPhysChem* **2012**, *13*, 3388–3396; d) M. V. Yigit, A. Moore, Z. Medarova, *Pharm. Res.* **2012**, *29*, 1180–1188; e) J. Kolosnjaj-Tabi, C. Wilhelm, O. Clément, F. Gazeau, *J. Nanobiotechnol.* **2013**, *11*, S7–S7; f) R. Ismail, G. Sulaiman, S. Abdulrahman, T. Marzoog, *Mater. Sci. Eng. C* **2015**, *53*, 286–297; g) M. K. Lima-Tenório, E. A. Gómez Pineda, N. M. Ahmad, H. Fessi, A. Elaissari, *Int. J. Pharm.* **2015**, *493*, 313–327; h) M. R. Santoso, P. C. Yang, *Stem Cells International* **2016**, *2016*, 9; i) H. N. Abdelhamid, *Materials Focus* **2016**, *5*, 305–323; j) E. Lasemi, N. Navi, R. Lasemi, N. Lasemi, in *A Textbook of Advanced Oral and Maxillofacial Surgery Volume 3* (Ed.: M. H. K. Motamedi), INTECH, **2016**, pp. 27–52.

[8] a) V. Amendola, P. Riello, S. Polizzi, S. Fiameni, C. Innocenti, C. Sangregorio, M. Meneghetti, *J. Mater. Chem.* **2011**, *21*, 18665–18673; b) V. Amendola, P. Riello, M. Meneghetti, *J. Phys. Chem. C* **2011**, *115*, 5140–5146; c) V. Amendola, M. Meneghetti, G. Granozzi, S. Agnoli, S. Polizzi, P. Riello, A. Boscaini, C. Anselmi, G. Fracasso, M. Colombatti, C. Innocenti, D. Gatteschi, C. Sangregorio, *J. Mater. Chem.* **2011**, *21*, 3803–3813; d) A. Kebede, A. Gholap, A. Rai, *World Journal of Nano Science and Engineering* **2011**, *1*, 89–92; e) P. Maneeratanasarn, T. V. Khai, B. G. Choi, K. B. Shim, *Korean Crystal Growth and Crystal Technology* **2012**, *22*, 134–138; f) P. Maneeratanasarn, T. V. Khai, S. Y. Kim, B. G. Choi, K. B. Shim, *Phys. Status Solidi* **2013**, *210*, 563–569; g) A. De Bonis, T. Lovaglio, A. Galasso, A. Santagata, R. Teghil, *Appl. Surf. Sci.* **2015**, *353*, 433–438; h) E. Fazio, *Colloids and Surfaces A: Physicochemical and Engineering Aspects* **2016**, *v. 490*, pp. 98–103-2016 v.2490; i) J. Xiao, P. Liu, C. X. Wang, G. W. Yang, *Prog. Mater. Sci.* **2017**, *87*, 140–220.

[9] a) A. Hanini, A. Schmitt, K. Kacem, F. Chau, S. Ammar, J. Gavard, *Int. J. Nanomed.* **2011**, *6*, 787–794; b) G. S. Demirer, A. C. Okur, S. Kizilel, *J. Mater. Chem. B* **2015**, *3*, 7831–7849; c) R. A. Revia, M. Zhang, *Mater. Today* **2016**, *19*, 157–168; d) J. Li, Y. Liu, R. Cha, B. Ran, K. Mou, H. Wang, Q. Xie, J. Sun, X. Jiang, *RSC Adv.* **2016**, *6*, 14329–14334.

[10] a) Jasmin, A. L. M. Torres, L. Jelicks, A. C. C. de Carvalho, D. C. Spray, R. Mendez-Otero, *Methods in molecular biology (Clifton, N. J.)* **2012**, *906*, 239–252; b) C. Corot, D. Warlin, *Wiley Interdiscip. Rev. Nanomed. Nanobiotechnol.* **2013**, *5*, 411–422; c) C. Corot, D. Warlin, *Wiley Interdiscip. Rev. Nanomed. Nanobiotechnol.* **2013**, *5*, 411–422; d) L. Li, W. Jiang, K. Luo, H. Song, F. Lan, Y. Wu, Z. Gu, *Theranostics* **2013**, *3*, 595–615.

[11] V. Patsulaa, M. Maksym, S. Dutz, D. Horák, *Phys. Chem. Solids* **2016**, *88*, 24–30.

[12] a) P. Reimer, M. Muller, C. Marx, D. Wiedermann, R. Muller, E. J. Rummeny, W. Ebert, K. Shamsi, P. E. Peters, *Radiology* **1998**, *209*, 831–836; b) G. Stoll, M. Bendszus, *Curr. Enzyme Inhib.* **2010**, *23*, 282–286.

[13] J. W. Bulte, I. D. Duncan, J. A. Frank, *J. Cereb. Blood Flow Metab.* **2002**, *22*, 899–907.

[14] a) A. Hatef, S. Fortin-Deschênes, E. Boulais, F. Lesage, M. Meunier, *Int. J. Heat Mass Transfer* **2015**, *89*, 866–871; b) X. Zhao, H. Zhao, Z. Chen, M. Lan, *J. Nanosci. Nanotechnol.* **2014**, *14*, 210–220.

[15] a) A. Ito, M. Shinkai, H. Honda, T. Kobayashi, *J. Biosci. Bioeng.* **2005**, *100*, 1–11; b) R. Ferrando, J. Jellinek, R. L. Johnston, *Chem. Rev.* **2008**, *108*, 845–910; c) M. De, P. S. Ghosh, V. M. Rotello, *Adv. Mater.* **2008**, *20*, 4225–4241; d) R. Ghosh Chaudhuri, S. Paria, *Chem. Rev.* **2012**, *112*, 2373–2433; e) K. McNamara, S. A. M. Tofail, *Phys. Chem. Chem. Phys.* **2015**, *17*, 27981–27995.

[16] S. Laurent, L. V. Elst, A. Roch, R. N. Muller, in *NMR-MRI, μSR and Mössbauer Spectroscopies in Molecular Magnets*, Springer Milan, Milano, **2007**, pp. 71–87.

[17] A. K. Singh, Q. Xu, *ChemCatChem* **2013**, *5*, 652–676.

[18] a) W. S. Seo, J. H. Lee, X. Sun, Y. Suzuki, D. Mann, Z. Liu, M. Terashima, P. C. Yang, M. V. McConnell, D. G. Nishimura, H. Dai, *Nat. Mater.* **2006**, *5*, 971–976; b) L. An, Y. Yu, X. Li, W. Liu, H. Yang, D. Wu, S. Yang, *Mater. Res. Bull.* **2014**, *49*, 285–290.

[19] P. C. Naha, A. A. Zaki, E. Hecht, M. Chorny, P. Chhour, E. Blankemeyer, D. M. Yates, W. R. Witschey, H. I. Litt, A. Tsourkas, D. P. Cormode, *J. Mater. Chem. B* **2014**, *2*, 8239–8248.

[20] H. Yang, X. Li, H. Zhou, Y. Zhuang, H. Hu, H. Wu, S. Yang, *J. Alloys Compd.* **2011**, *509*, 1217–1221.

[21] a) H. Yang, J. Zhang, Q. Tian, H. Hu, Y. Fang, H. Wu, S. Yang, *J. Magn. Magn. Mater.* **2010**, *322*, 973–977; b) S. Liang, Q. Zhou, M. Wang, Y. Zhu, Q. Wu, X. Yang, *Int. J. Nanomed.* **2015**, *10*, 2325–2333.

[22] J. Lu, S. Ma, J. Sun, C. Xia, C. Liu, Z. Wang, X. Zhao, F. Gao, Q. Gong, B. Song, X. Shuai, H. Ai, Z. Gu, *Biomaterials* **2009**, *30*, 2919–2928.

[23] H. Wu, G. Liu, X. Wang, J. Zhang, Y. Chen, J. Shi, H. Yang, H. Hu, S. Yang, *Acta Biomater.* **2011**, *7*, 3496–3504.

[24] a) J. Zhang, D. N. Oko, S. Garbarino, R. Imbeault, M. Chaker, A. C. Tavares, D. Guay, D. Ma, *J. Phys. Chem. C* **2012**, *116*, 13413–13420; b) R. G. Nikov, N. N. Nedyalkov, A. S. Nikolov, P. A. Atanasov, M. T. Alexandrov, D. B. Karashanova, *Vol. 9447*, **2014**, pp. 94470 M-94470 M-94477; c) C. Lee, N. R. Kim, J. Koo, Y. J. Lee, L. Hyuck Mo, *Nanotechnology* **2015**, *26*, 455601; d) Z. Swiatkowska-Warkocka, A. Pyatenko, F. Krok, B. R. Jany, M. Marszalek, *Sci. Rep.* **2015**, *5*, 9849; e) P. Wagener, J. Jakobi, C. Rehbock, V. S. K. Chakravadhanula, C. Thede, U. Wiedwald, M. Bartsch, L. Kienle, S. Barcikowski, *Sci. Rep.* **2016**, *6*, 23352.

[25] M. A. Koten, P. Mukherjee, J. E. Shield, *Part. Part. Syst. Charact.* **2015**, *32*, 848–853.

[26] M. Kaur, J. S. McCloy, R. Kukkadapu, C. Pearce, J. Tucek, M. Bowden, M. Engelhard, E. Arenholz, Y. Qiang, *J. Phys. Chem. C* **2017**, *121*, 11794–11803.

[27] D. Werner, S. Hashimoto, T. Tomita, S. Matsuo, Y. Makita, *J. Phys. Chem. C* **2008**, *112*, 1321–1329.

[28] N. Haram, N. Ahmad, *Appl. Phys. A* **2013**, *111*, 1131–1137.

[29] D. Dorranian, A. F. Eskandari, *Mol. Cryst. Liq. Cryst.* **2015**, *607*, 1–12.

[30] a) V. Kotaidis, A. Plech, **2005**, *87*, 213102–213101; b) A. Plech, V. Kotaidis, M. Lorenc, M. Wulff, *Chem. Phys. Lett.* **2005**, *401*, 565–569; c) S. Ibrahimkutty, P. Wagener, T. d. S. Rolo, D. Karpov, A. Menzel, T. Baumbach, S. Barcikowski, A. Plech, *Sci. Rep.* **2015**, *5*, 16313; d) A. Resano-Garcia, Y. Battie, A. Koch, A. En Naciri, N. Chaoui, *J. Appl. Phys.* **2015**, *117*, 113103–113101.

[31] G. Askaryon, E. M. Morez, *JETP Lett.* **1963**, *16*, 1638–1963.

[32] a) S. Barcikowski, V. Amendola, G. Marzun, C. Rehbock, S. Reichenberger, D. Zhang, B. Gökce, *Handbook of Laser Synthesis of Colloids*, **2016**; b) V. Amendola, M. Meneghetti, *Phys. Chem. Chem. Phys.* **2013**, *15*, 3027–3046.

[33] A.-A. El Mel, R. Nakamura, C. Bittencourt, *Beilstein J. Nanotechnol.* **2015**, *6*, 1348–1361.

[34] a) Y. Jee, M. F. Becker, R. M. Walser, *J. Opt. Soc. Am. B* **1988**, *5*, 648–659; b) J. Krüger, W. Kautek, *Adv. Polym. Sci.* **2004**, *168*, 247–289.

[35] a) R. Diaz-Uribe, M. Rosete-Aguilar, R. Ortega-Martinez, *Rev. Mex. Fis.* **1993**, 484–492; b) M. González-Cardel, P. Arguijo, R. Díaz-Uribe, *Appl. Opt.* **2013**, *52*, 3849–3855.

[36] C. Gammer, C. Mangler, C. Rentenberger, H. P. Karnthaler, *Scr. Mater.* **2010**, *63*, 312–315.

[37] X. Yibin, Y. Masayoshi, V. Pierre, *Jpn. J. Appl. Phys.* **2011**, *50*, 11RH02.

Manuscript received: November 10, 2017
Version of record online: May 3, 2018